ANNALI DI GEOFISICA, VOL. 42, N. 5, October 1999

An integrated study of physical precursors of failure in relation to earthquake prediction, using large scale rock blocks

Kamel Baddari ([1]), **Guennadi A. Sobolev** ([2]), **Anatoli D. Frolov** ([3]) **and Alexander V. Ponomarev** ([2])
([1]) *Laboratory of Physics of the Earth, University of Boumerdes, Algeria*
([2]) *Institute of Physics of the Earth, Russian Academy of Sciences, Moscow, Russia*
([3]) *Geophysical Division, NCG, Moscow, Russia*

Abstract
This paper is multi-analysis approach to rock failure using metric size rock samples. The use of large-scale models permits simulation of the seismic process (including internal rupture on several scales) and utilization of a dense network for observation of the spatial variations of several physical parameters. The experiments were performed both on solid rock blocks and on concrete blocks with artificial defects, which enabled simulation of internal shear fracture. The number of various precursors appears to rise up to failure, all of them clearly manifest at the stage of a rapid drop in the applied stress (unstable deformation). The experiment suggests that rocks under strain and prior to failure must be characterized by a heterogeneous field of strains. This means that the strain is distributed mosaically, dilatancy does not generate uniformly and areas where it occurs are likely to be stucturally mosaic themselves. To reinforce the prediction of micro- and macrofailure, we have realized simultaneous processing of the obtained data, using sophisticated multidimensional orthogonal functions to represent the different precursors. The possibility to identify the early stages of microfailures and to predict the macrofailure by means of statistical complex parameters derived from data on local deformations, acoustic emissions, elastic waves velocities, electric resistivity and self electric potentials is shown. Despite a considerable dissimilarity in mechanical properties of granite basalt and concrete, the complex parameter proves morphologically identical. Parameter S_1 reveals exponential rise up to failure in all cases, and parameter S_2 is bay-shaped in form, which makes it more promising in terms of prognosis.

Key words *precursors – simulation – failure – complex parameter – prediction – earthquake*

1. Introduction

Since the acquisition of field data on the seismic process is slow, and the physical phenomena in earthquake sources are difficult to investigate *in situ*, one has to use laboratory experiments to simulate earthquakes and rock bursts.

Each rock is characterized by a specific crystalline textural structure, with some strength distributions of grain contacts, grain interiors and intergrain zones. The processes of deformation and failure of such a structure under load are accompanied by changes of these distributions caused by destruction of bonds at the weakest contacts and formation of microfractures. In real rock masses, these changes are not uniform in space and time and can sometimes be anisotropic, which makes control of the state of the deformed rock mass more difficult.

Mailing address: Prof. Kamel Baddari, Laboratory of Physics of the Earth, University of Boumerdes, Bat. 19 G4, Boumerders 35000, Algeria.

The physical subsystems (Baddari and Frolov, 1995; Frolov, 1986) associated with the spatial crystalline structure of a rock sample are conditioned by the response to external mechanical influences. The changes in the spatial structure are accompanied by certain changes in mechanical, electrical and other properties of the medium, most of which can be recorded by remote sensing methods. Physical precursors of rock fracturing have been studied for a long time and some progress has been achieved (among others see Scholz *et al.*, 1972; Rice, 1983; Savich, 1983-1984; Baddari *et al.* 1988; Horowitz and Ruina, 1989; Meredith *et al.*, 1990; Ohnaka and Kunwahara, 1990; Sobolev and Asatrian, 1990; Zhaoyong *et al.*, 1990; Lei *et al.*, 1991; Lockner *et al.*, 1991; Lockner and Byerlee, 1991; Sobolev, 1993; Baddari and Frolov, 1997).

The experiments reported here were performed on solid rock blocks and on concrete blocks with artificial defects acting as stress concentrators. New here is the use of large samples, which allows some spatial resolution of the precursory behaviour. The large size also allows monitoring of several parameters simultaneously, namely: local surface strain, acoustic and electromagnetic emissions, ultrasonic elastic wave velocity and amplitude, electrical conductivity and electric- self-potential.

A question arises whether it is at all possible to reliably identify a macrofailure precursor by means of a complex analysis of a number of physical parameters. It would be desirable to reinforce this approach with a multi-dimensional mathematical analysis.

2. Experiments on unfractured granite and basalt

A petrographic analysis of the granite block gave its composition as quartz and albite (40%), biotite (up to 20%) and accessory admixtures of pyrite, muscovite and corundum. The grain size in quartz was up to 2 mm, in the other components up to 1 mm. The basalt block contained plagioclase (60%), olivine (20%), monoclinic pyroxene (10%), augite, diopside, ilmenite and apatite (10% all told). The bulk porosity was 6%, the grain size under 1.5 mm. Granite and basalt cubes as large as 1 m^3 were loaded cyclically under uniaxial loading (*i.e.* confining pressure = 0). We performed 8 and 5 cycles, respectively, for granite and basalt blocks with the maximum load of each cycle increasing progressively. A cycle lasted 6 to 10 h. The specimen was unloaded after each cycle. The final failure load P_f was 140 MPa for the granite and 75 MPa for the basalt blocks. The authors list five basic guidelines that allow, with some approximation, failure mechanics to be applied towards an earthquake source:

1) A tectonic earthquake source is the fracture of the earth's material along a (plane) surface.

2) Fracture results from (shear) stress, which accumulates during tectonic deformation, and leads to total or partial stress release over the fracture area.

3) Fracture is initiated over a small area and then propagates at a velocity not exceeding the velocity of longitudinal waves.

4) Fracture corresponding to the tectonic earthquake source is a shear fracture ; that is, the normal displacement jump is negligible.

5) The material surrounding the fracture surface remains linearly elastic.

2.1. *Local strain*

A system of rosettes of 50 mm wire strain gauges were cemented to a lateral face of the block to measure local strain. The relative strain readings were measured from vertically fixed ε_i, horizontally fixed ε_j and set at 45° ε_{ij}; pick ups were used to compute the first invariant I of the plane strain tensor $I = \varepsilon_i + \varepsilon_j$ and shear deformation $\gamma = (\varepsilon_i + \varepsilon_j)^{-2}\varepsilon_{ij}$. The absolute errors in measuring I and γ were 6×10^{-5} and 10.3×10^{-5} respectively. Parameter I characterizes the relative changes in the surface area of a block element. Figure 1a,b shows the results of the experiment with the basalt block. Figure 1a shows the positions of the different strain gauges and macrocrack routes. Figure 1b shows the 1st flat strain tensor invariant for rosettes 6, 13 and 18, the former in the area unaffected by macrocracks, the last two in its path. Positive deviations from the Y-axis point to the element square contraction, while negative-dilatancy. Starting from

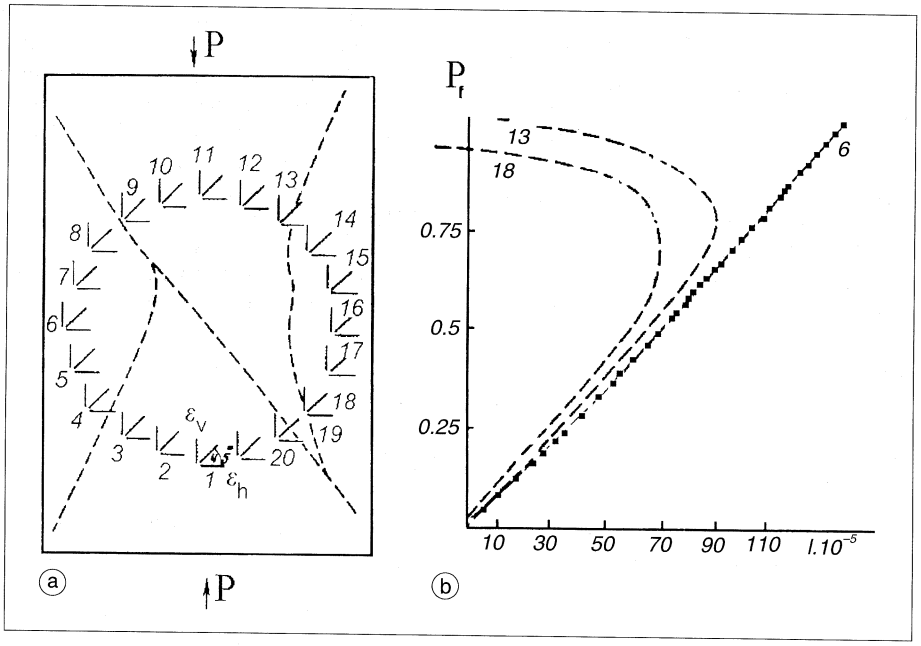

Fig. 1a,b. Positions of the strain gauges on the block of basalt (a) and the variations of the first invariant I of the plane strain tensor for the strain gauges 6, 13 and 18 (b). The dash lines in (a) represent the traces of the principal macrofailure.

$F/S \approx 0.75(F/S)_f$, graphs of rosette 18 and 13 demonstrate dilatancy. However, a linear increase in parameter I characterized the rosette 6 situated far from the macrorupture. The data of the other rosettes were similar. The experiment shows that a heterogeneous field of strains must characterize rocks under strain and prior to failure.

2.2. *Acoustic emission*

Acoustic Emission (AE) by rock samples in failure reflects the process of crack formation and can be viewed, with a certain allowance, as an analogue of global seismicity. Eight piezoelectric ceramic sensors were installed on the granite block, two on each free face. The signals were recorded by a digital oscillograph with a scanning rate of 50 ns per point.

In each subsequent cycle of loading, the acoustic activity dramatically increased after the

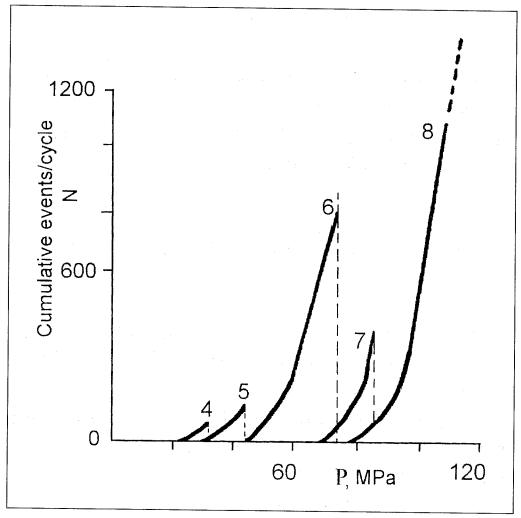

Fig. 2a. The cumulative acoustic emission activity as a function of stress for the last five loading cycles.

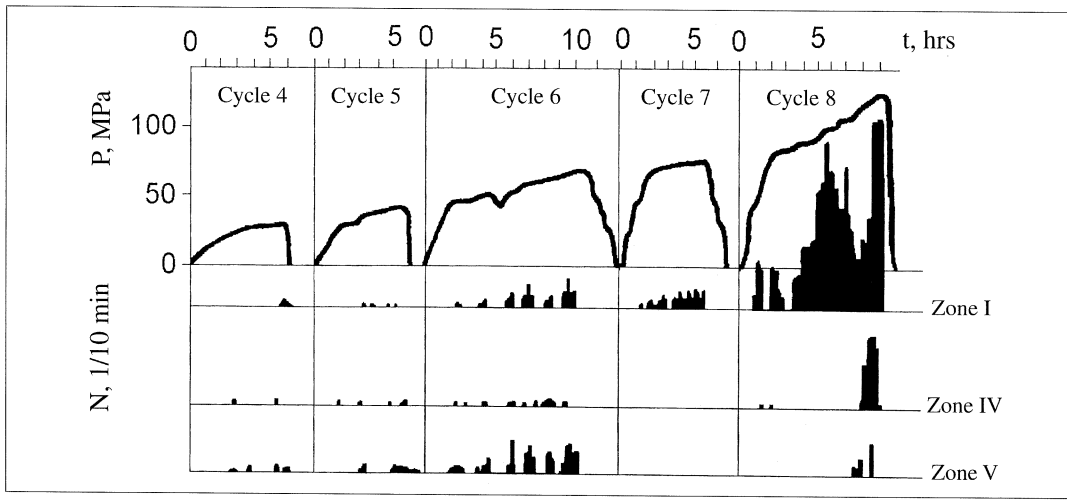

Fig. 2b. The stress history and acoustic emission activity for three distinct zones within the granite sample. The diagram of the position of zones I, IV, and V is in the right top corner.

maximum load of the previous cycle had been reached (*i.e.* Kaiser effect). The number of AE signals was abnormally small in the 7th loading cycle (fig. 2a). This suggests a nonuniform distribution of AE sources and nonsimultaneous acoustic activation of different portions of the block. This interpretation was corroborated by the results of locating more than 3500 AE signals. The coordinates of the hypocenter sources were calculated according to a traditional seismological technique by the difference in AE signal recording time (Sobolev, 1993). The uncertainty in determining the coordinates of the hypocenters were 2-3 cm, that is, about 4 percent of the linear block dimension. Differences were noted in the distributions of activity as a function of time for the different zones of the block. Figure 2b shows the distribution of AE signals over the three principal zones of acoustic activity in the granite block. The number of signals in the most active zone 1 gradually increased with increasing load and reached its peak before failure. At the same time, zone 4 and, especially, 5 appear to have three acoustic stages: rises in intensity in cycles IV-VI, decay in cycle VII and recurrent rise in cycle VIII. A period of complete «quiescence» occurred in the 7th cycle (fig. 2b).

2.3. *Velocity of ultrasonic waves*

Each free face of a block was instrumented with 9 piezo-electric compressional transducers with a free resonance frequency of 90 kHz. They were used as focuses and receivers of ultrasonic signals. The number of monitored paths was 96, enabling one to study velocity variations in separate portions of the block. The uncertainty in measuring *P*-wave arrival times was about 0.7 percent and that for the amplitude was 10 percent. It was found that, above about one half of the failure strength the average velocity became a non-linear function of the load. In particular, the velocity reached a maximum when loading was one-half the maximal, possibly due to the developing dilatancy. Figure 3a shows the values of σ the mean square velocity deviation, measured along the X and Y axes at different loads. The calculation was performed for the 48 paths in each direction. The velocity variance significantly increased for loads increasing from about 0.8 P_f up to the final failure load. It can be seen that increase in stress was accompanied by increased velocities scatter.

To evaluate the evolution of the velocity inhomogeneities, the block was partitioned into 27 elementary volumes Δv_i. The velocity V_i in

each volume ΔV_i was calculated using the formula

$$V_i = (\Sigma V_j)/n. \qquad (2.1)$$

Where V_j is the velocity along the rays crossing the volume $\Delta v_i (i = 1, 27)$.

Velocity contrasts of each element δV_i *versus* mean velocity V_a in the block were estimated

$$\delta V_i = [(V_i - V_a)/V_a] \cdot 100\%. \qquad (2.2)$$

Velocity variations of both signs up to a few percent were recorded in the final stage of loading. Simultaneous changes with opposite signs frequently occur in adjacent elements and even within a single element, but in different directions.

Figure 3b demonstrates the behaviour of velocity variations for sets of elements (4-6, 13-15, and 22-24) of the central block cross-section. One can clearly see that in the upper part of the block δV_i increases with an increase in F/S. Considering that the velocity in the entire block has a tendency to decrease with increase in stress, such change in δV_i testifies to a slower fall of velocity in these elements compared to the entire block, *i.e.* crack formation is less intense. As the lower part (element 22, 23, 24), δV_i is the smallest and, on the whole, continues to fall, *i.e.* crack formation is more intense than the average for the entire block. Thus, the middle part of the block is apparently a zone of transition between the lower part characterized by intense cracking and the higher part of the block where the cracking is practically negligible. To sum up, the velocity contrast in different regions of the block increases and reaches a maximum at failure.

Unlike the basalt block, the granite specimen was characterized by a certain anisotropy of velocities in the directions X and Y, perpendicular to the direction of the load F. The average velocities before loading were $V_{a(x)} = 5.17$ km/s and $V_{a(Y)} = 4.87$ km/s. After loading they became 4.84 km/s and 4.47 km/s respectively. One example of the anisotropy of velocity is shown in fig. 3c. The disposition of the 27 elements was the same as for both the granite and basalt block.

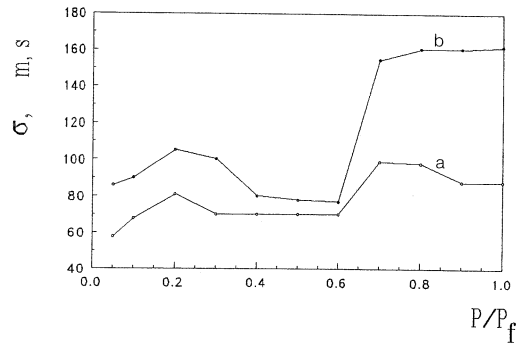

Fig. 3a. The variation of the variance of the elastic wave velocities measured in the direction X (a) and Y (b) as a function of the normalized load through the granite block.

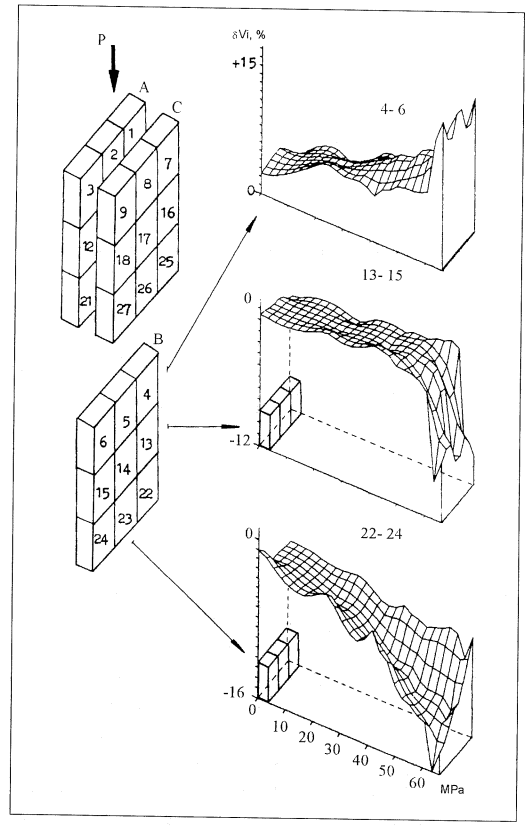

Fig. 3b. The percentage difference between the average velocity and those in the interior elements 4-6, 13-15 and 22-24 of layer B in the basalt block.

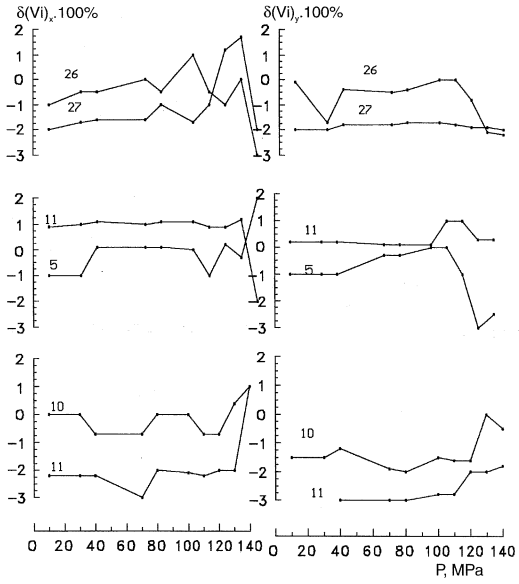

Fig. 3c. Example of longitudinal local velocity anisotropy in the elements 1, 5, 11, 26 and 27 in the directions *X* and *Y*.

The observed velocity anisotropy was found to be associated with changes in microcracks density and distribution pattern. The anisotropy tended to increase just before the main rupture. The peak of this increase coincided with the dynamic propagation of the rupture.

2.4. *Self-potential*

The sensors of electric potential were non-polarizable chlorine-silver electrodes. They were placed on the free faces of the specimen. There were as many as 40 of these in some of the experiments, enabling one to study the structure of the electric field in detail. The intrinsic drift of the electrode potentials did not exceed 0.7 mV for a complete loading cycle. The background values had been estimated prior to the experiment by carrying out an areal survey of surface potentials on a 7 × 7 cm grid on all faces of the specimen.

Rather surprising was the presence of an appreciable spontaneous electric field in the intact specimen reflecting certain petrographic features (*i.e.* presence of biotite). Repeated measurements showed that the field was quite stable in time, its fluctuations being below 2 mV. As the block was loaded, the spontaneous electric field changed significantly. Maps of isopotential lines show examples of the initiation and disintegration of local electric anomalies when the load varied in the range 30 to 75 MPa. One of the anomalies began to form at a load of 20 MPa, reached a maximum of about 30 mV at 55 MPa, and then relaxed down to the background values over the period of several hours. The load was continuously increased during that time (fig. 4). The appearance of the anomaly coincided in time with the formation of a shallow AE source near it (see fig. 2b, zone 5).

After loading, the variations of the surface electric field significantly decreased. The disappearance of anomalous regions during load removal occurred with a lag of several tens of minutes. This indicates a nonlinear relation between the mechanical and electric fields. A number of features observed in the electric disturbances seem to be explainable qualitatively

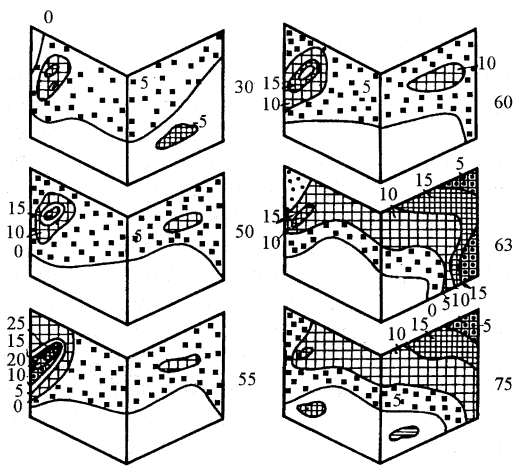

Fig. 4. The iso-potential contour maps for two planes of the granite sample, constructed for different axial stresses (30-75 MPa). Numbers at isolines represent potential values in mV, relative to «zero» electrode.

within the framework of ionic migration mechanisms. The dynamic of increase and of relaxation of electric potential ΔU (these stages last 10 min) does not correlate with the variation of the load and in our opinion reflects the irregular process of rupture in the rock.

The existence of a primary potential in a large heterogeneous block is linked to the evolution of the potentials of adsorption-diffusion, commonly found in various geological settings. The stability of the field is determined by a stationary condition of the process of ionic migration. The occurrence of ruptures in the block destroys the stationary regime of the process.

2.5. *Electric resistivity*

The variations of apparent electric resistivity were studied using direct current and four-electrode devices in different orientations (fig. 5a). The receiving dipoles were various combinations of the nonpolarizable sensors mentioned above. This strength enabled us to evaluate relative changes in of resistivity both in the entire block and in separate portions of it. The uncertainty of measuring the variations of resistivity was below 5 percent.

Large local variations of apparent resistivity were detected. For example, in certain zones, resistivity anisotropy was found to develop with time (*i.e.* an increase in resistivity in one direction corresponded to a decrease in the perpendicular direction). The relevant curves are shown in fig. 5b. One can see that the greatest variations are recorded in the 6th loading cycle, their relative value reaching 60% of the variations of the resistivity. The length of the perpendicular receiving dipoles 1-3 and 3-5 was 15 cm. However, resistivity variations were much smaller for line 7-8, which was parallel to dipole 1-3, but was 50 cm long. The anisotropy can be qualitatively explained by the development of oriented sets of oriented cracks. This is indirectly confirmed by the results of AE observations indicating a zone of increased acoustic activity in that region (zone 5, fig. 2b). It is in that same region that a local anomaly of self-potential appeared.

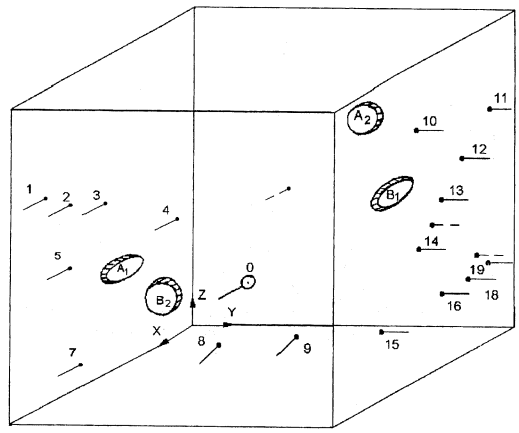

Fig. 5a. Arrangement of the receiving electrodes and the feeding electrodes (AB) on the granite sample. O - zero electrode.

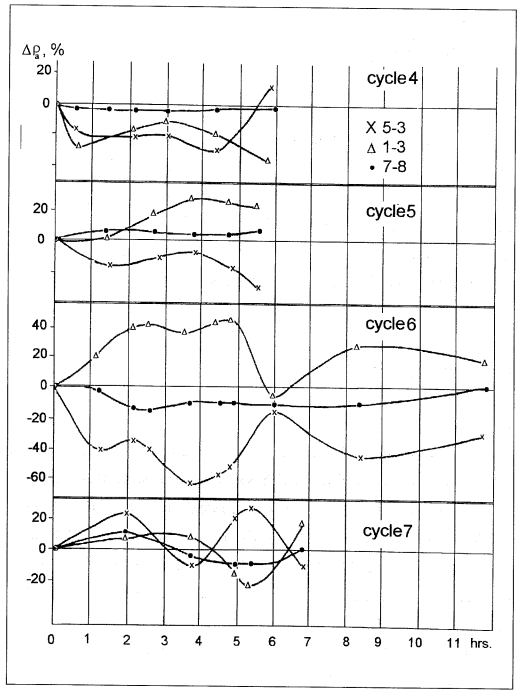

Fig. 5b. Variations of the apparent electrical resistivity for different pairs of electrodes during four loading cycles.

3. Experiments on concrete blocks having artificial stress concentrators

The next step in experimentally simulating earthquake preparation was to conduct experiments in concrete specimens with internal stress concentrators in the shape of two pairs of glass plates. The sample was prepared out of fine-grained granite (40%), quartz sand (20%), cementum 500 (25%) and water (8%), and cut under and rectangular prism 2000 × 1000 × 500 mm in size. The stress concentrators had been inserted under an angle of 35° with respect to the loading axis (fig. 6). We note that this arrangement could be regarded as a simulation of a seismic gap. A set of sensors was installed in the region between the concentrators to record local deformation, acoustic emission, velocities of ultrasonic waves, electrical potential and variations of electric resistivity. The process involved four loading cycles (fig. 6). The rupture load P_f was 15 MPa.

The study of the local strain shows (fig. 7) that the dilatancy migrated from the limits of the concentrators towards the middle of the block. On the *Y*-axis the value of the 1st flat strain tensor invariant for each element is plotted, and on the *X*-axis- the time of the 4th, final cycle. Each graph of fig. 7 shows the variation of parameter *I* in the corresponding element during the rupture of the barrier. The shaded elements are those in which a strain precursor was observed (the transition of *I* by an extremum). They are characterized by a short transition from compression to dilatancy. Also rather mosaic looking is the strain field of the maximal compression. It was noticed that failure was preceded by a reversal in graphs I of elements showing progressing dilatancy, *i.e.* dilatancy was decreasing towards the core of the sample. This leads us to believe that the non uniformity of a stress-strain state even in originally rather homogeneous materials, may increase under strain, due to changes in their properties in the vicinity of different-scale fracturing as shown in fig. 7.

Figure 8 shows the typical variation of the number of acoustic pulses per unit of time *N*, normalized to their ultimate values. The graph N/N_{max} clearly shows three stages: I - rise in acoustic intensity; II - acoustic quiescence and

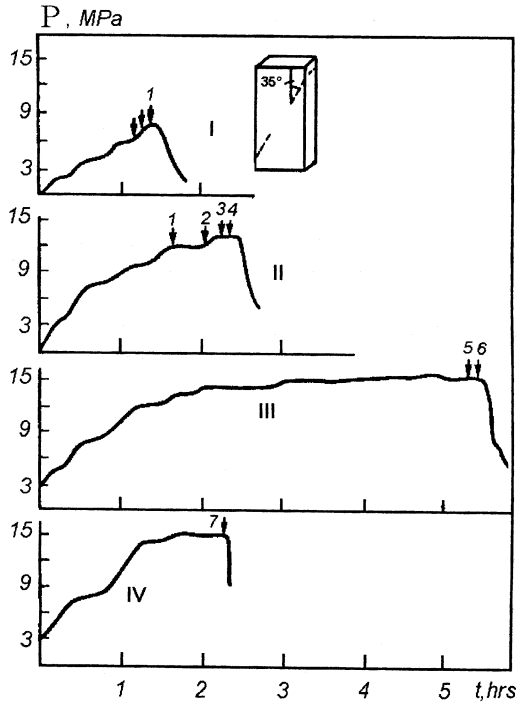

Fig. 6. The loading history of the concrete block (I- IV: loading cycles). Outlined in the right top corner is a diagram of the positions of the glass concentrators. The arrows denote the times when the fractures reached the free surface.

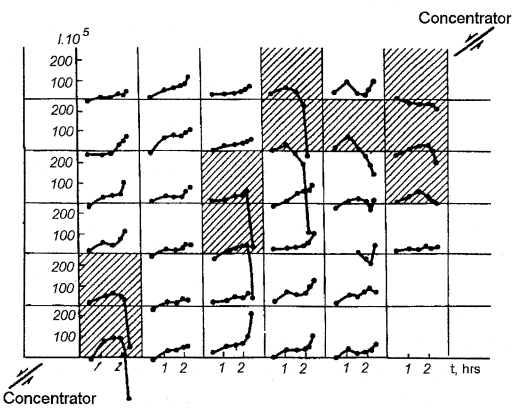

Fig. 7. The curves of the variations of the first invariant of the plane strain tensor for different stain gauges during the loading cycle 4. The shaded areas indicate the macrorupture zones.

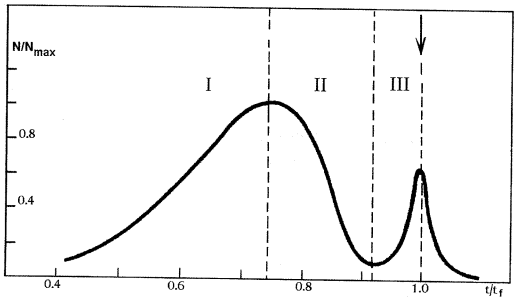

Fig. 8. The acoustic emission intensity N normalised by the maximum acoustic emission intensity N_{max} recorded in the concrete block. The arrow indicates the time of principal macrofailure.

III - renewed intensity prior to failure. Stage I proceeds against the background of increasing load and corresponds to the stage of small cracks accumulation. Stage II is observed in the area of maximal stresses and takes up most of the cracks growth stage and the beginning of their concentration in the area of an incipient macrofailure. Stage III develops against a failing stress and the main rupture taking shape.

The diagram of the positions of the ultrasonic emitors and receivers on two opposite faces (I and III) is shown in fig. 9. All the rays are inclined at 45° with respect to faces I and III. The P and S wave arrival times did not significantly change in the stable zones of the block. The ratio t_S/t_P showed practically no change during the experiment. In the zone of shearing rupture, we noticed a strong variation of t_P and t_S and of the amplitudes A_P and A_S. The path 5-3, passing through the barrier zone, showed a strong variation of the wave arrival times and amplitudes. t_P increased by 5%, t_S by 4% and t_S/t_P decreased by 2% at the end of the third cycle. A_P has decreased by a factor of 4 and A_S by 2. At the end of the third cycle, just before $P = 15$ MPa, the rupture process intensified in the barrier zone. This variation of t_S/t_P and A_P/A_S is a precursor of the formation of the macrofailure between the stress concentrators. For the pairs of paths 7-6 and 9-7, and, 13-11 and 14-12, the parameters of the elastic waves behave differently. Thus, we can say that the rupture occurs

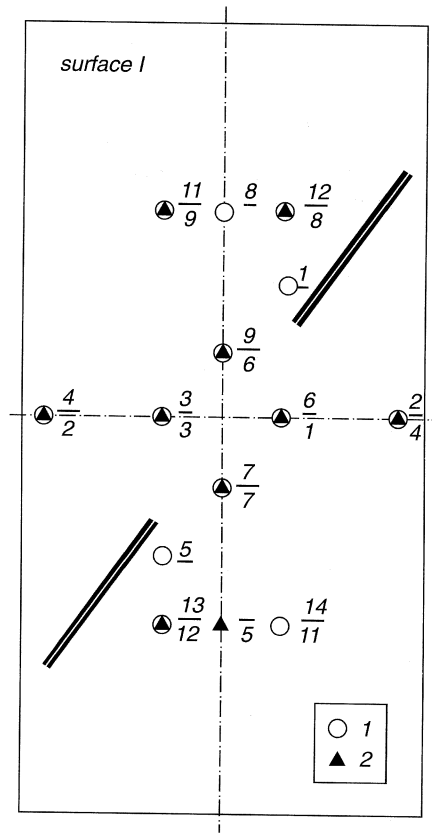

Fig. 9. The location of the ultrasonic emitors (1) on face I and receivers (2) on face II of the concrete block. Position of stress concentrators are also shown.

differently in the various regions of intersection of these paths. During the fourth cycle, t_S/t_P and A_P/A_S changed strongly for the paths 13-11 and 3-1. This process during the fourth cycle gave rise to the principal macrofailure between the stress concentrators.

The behaviour of the path 3-1 (fig. 10) presented broad anomalies during cycles II and III. The analysis of the ratio A_P/A_S and t_S/t_P shows that the rupture of the barrier started during the third loading cycle, and it migrated towards the center of the barrier during the fourth cycle of the experiment.

The variation of the apparent electrical resistivity $\Delta\rho$ in the zone of formation of the ma-

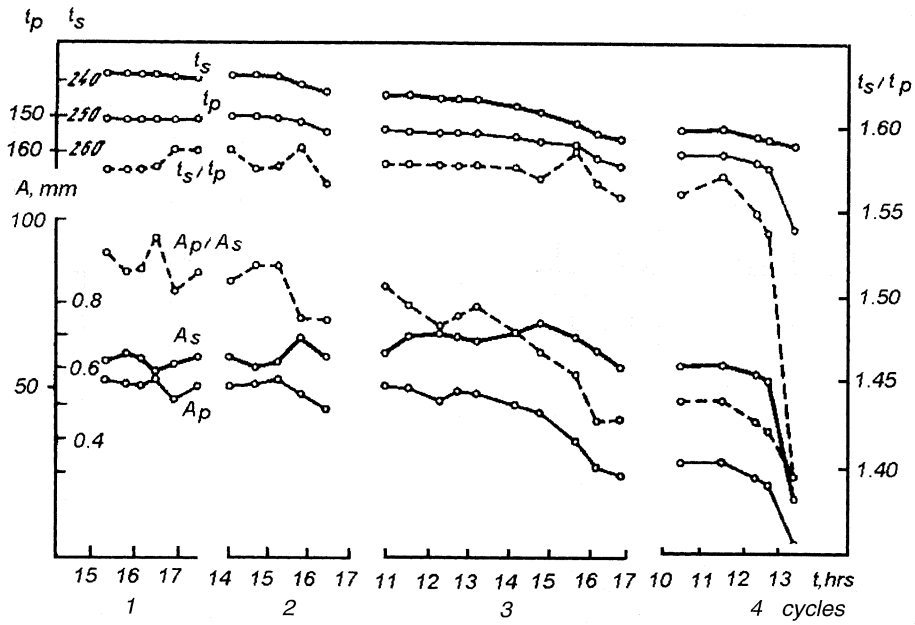

Fig. 10. Travel times t_S, t_P and amplitudes A_P, A_S and the A_P/A_S ratio for path 3-1(note that path 3-1 goes throuh the barrier).

crorupture is large and is often characterized by an opposite sign to that of $\Delta\rho$ recorded in the exterior zones. When stress applied to the sample increased in the 1st, 2nd, and 3rd cycles up to the moment when it reached 15 MPa, almost all routes revealed a monotonously decreasing electric resistivity that could be due to expansion of a conducting paths system in a room humidity experiment and crack accumulation within the sample. Most pronounced variations were recorded in the 3rd cycle, when the stress was closing on the maximum. The dispersion of $\Delta\rho$ increases as we approach the macrofailure. Figure 11 shows examples of variations of $\Delta\rho$ during the rupture preparation. The measurement paths, located in the middle of the block between the stress concentrators, showed an exponential increase in $\Delta\rho$ during the fourth cycle. The increase in $\Delta\rho$ during the last stage of the experiment is probably caused by coalescing ruptures and the formation of the macrorupture. The routes which passed through the top and the bottom of the model outside the area of the main rupture formation show recovery of resistivity during an important stage of the experiment 7.5 h after the start. Considering that stress during that stage was decreasing, this change could be due to closure of earlier microcracks. Data obtained in the present work and in the course of other similar tests (Baddari and Frolov, 1995,) allow us to conclude that electrical resistivity variations in the area of an incipient macrocrack are by far greater in value, and often of the opposite polarity compared with the external zone variations. The variation amplitudes for short bases are more pronounced than for long ones, *i.e.* the scale effect is apparent-variations scatter over different routes increases before failure.

Figure 12 shows the graphs of variations of electric potentials of the electrodes 11 and 10 during the experiment. The potential decreased from the beginning to the end of the experiment by about 500 mV. The step-like increase of the potential corresponds to the beginning of the microruptures. When ΔU remained constant, we

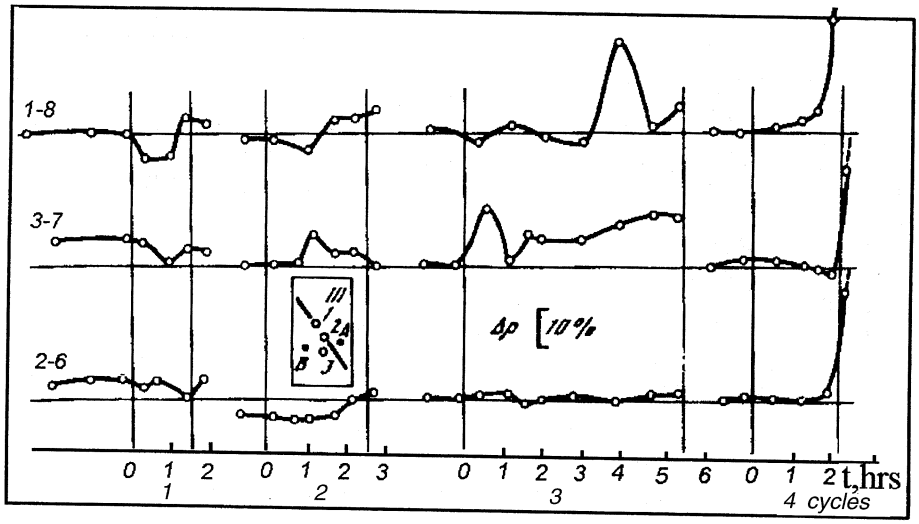

Fig. 11. Variations of electric resistivity in the top zone (1-8) and the low zone of concentrators (2-6) and in the low zone of concrete block (3-7). The position of electrodes 1, 2, 3 on face III is shown on the diagram. The electrodes 8, 6, 7 were located on side I. The feeding electrode B was on side III, electrod A on side I.

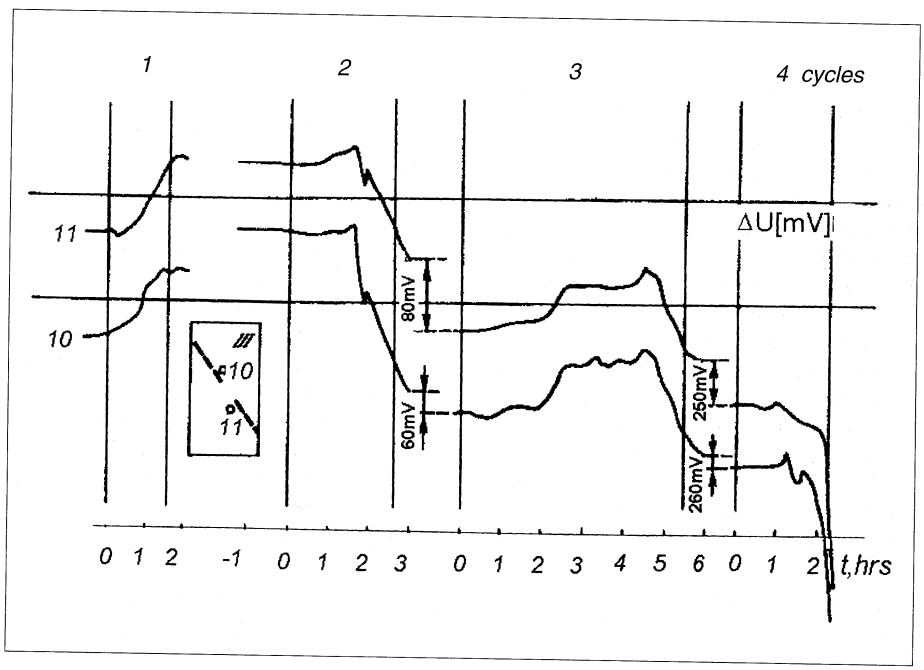

Fig. 12. Variations of the electric potential with respect to the ground for the electrodes 10 and 11.

did not observe ruptures occurring at higher scales. The fast transition of the rupture to high scale, which led to the formation of the macroruptures and to the redistribution of stress in the block, corresponded to an important variation of the electric field. This process repeats itself in the interval 14-15 MPa at the third cycle of loading. A characteristic decrease of ΔU was observed during the macrofailure process of the barrier at the end of the fourth cycle.

The variations of ΔU are due to the evolution of the failure process. The rate of increase in ΔU is higher than the rate of change of the strain in the zone of preparation of the principal rupture.

Observation and analysis of all the precursors have enabled us to forecast the time of main rupture to within half an hour. The last precursors to be observed (strain and electrical ones) were recorded a few minutes before the final failure. The maximum applied strain rate during the final loading stage was maintained constant, at about 10^{-8} s^{-1}. Under the conditions prevailing in the Earth's crust, the rate of strain in seismically active regions is in the order of 10^{-14} s^{-1}. Such values have been recorded, for example, in the Garm (Tadjikistan) test Area (Sobolev, 1993). The uncertainty in forecasting the time of rupture, extrapolated from our experiment to the crustal scale, would be in the order of a few years to a few months. The set of precursors we have recorded can thus be classified as long-and medium-term ones.

The Stress-Strain State (SSS) of the crust is far from uniform. There is no doubt that this has to do with lithologic differences and faults. Field observations reproduce only an on-the-spot picture of field of strain, therefore laboratory simulation is desirable for the investigation of SSS variability in time. The experiment suggests that rocks under strain and prior to failure must be characterized by a heterogeneous field of strains. The dependance of a precursor amplitude on epicentral distance is hard to define because of a great data scatter. On the face of it, the latter is largely due to structural discreteness of the Earth's crust, inhomogeneity of the stress-strain field and precursors' parametrical properties. All this emphasises the importance of simultaneous use of all types of precursors.

4. Statistical analysis of the results using multidimensional orthogonal functions to represent the different precursors

Five physical parameters were considered as principal ones: the first invariant of the plane strain tensor (I); elastic longitudinal wave velocity (V); number of acoustic emissions (N); electrical resistivity $\Delta\rho$ and electrical potential changes ΔU.

For analyzing and treating the raw data the method of natural orthogonal functions was chosen (Baddari *et al.*, 1988; Nikitin, 1993).

Let the data $y(P, x)$ be presented in the form of matrix

$$\begin{Vmatrix} y_{11} & y_{12} \cdots y_{1n} \\ y_{21} & y_{22} \cdots y_{2n} \\ y_{m1} & y_{2m} \cdots y_{mn} \end{Vmatrix}$$

where y_{ij} the observed value of the jth geophysical field at the indication of pressure where $j = 1, ..., n$ with n being the number of physical parameters, and $j = 1, ..., m$).

We are going to approximate the function $y(P, x)$ in the following form:

$$y_n(P, x) = \sum_h S_h(P)\Phi_h(x). \qquad (4.1)$$

The error $\delta_n(P)$ of this approximation is given by

$$\delta_n(P) = [y(P, x) - y_n(P, x)]. \qquad (4.2)$$

The function $S_h(F/S)$ and $\Phi_h(x)$ must produce an optimal fit, that is to say

$$\delta_n(P) = \sum_P \sum_x [y(P, x) - \qquad (4.3)$$

$$-\sum_h S_h(P)\varphi_h(x)]^2 = \text{Min.}$$

Using

$$y(P, x) = y_{ij}$$

$$\varphi_h(x) = \varphi_{hj}$$

$$S_h(P) = S_{ih}$$

we obtain

$$\delta_n = \sum_i \sum_j [y_{ij} - \sum_h S_{ih} \varphi_{hj}]^2 = \text{Min.} \quad (4.4)$$

The functions S_{ih} and Φ_{hj} will be computed in the special case where the sum over h has only one term. We obtain

$$\delta_n = \sum_i \sum_j [y_{ij}^2 - 2 \sum_i \sum_j y_{ij} S_i \varphi_j + \\ + \sum_i S_i^2 \sum_j \varphi_j^2. \quad (4.5)$$

According to the condition of a minimum error, we get the following system of $m + n$ equations:

$$\frac{\partial \delta_n}{\partial S_i} = -2 \sum_j y_{ij} \varphi_j + 2 S_i \sum_j \varphi_j^2 = 0 \\ (i = 1,2,\ldots m) \quad (4.6)$$

$$\frac{\partial \delta_n}{\partial \varphi_j} = -2 \sum_i y_{ij} S_i + 2 \varphi_j \sum_i S_i^2 = 0 \\ (j = 1,2,\ldots n).$$

This leads to

$$\sum_j y_{ij} \varphi_j = S_i \sum_j \varphi_j^2 \quad (4.7a)$$

$$\sum_i y_{ij} S_i = \varphi_j \sum_i S_j^2. \quad (4.7b)$$

Replacing j by k in (4.7a), we get

$$S_i = \frac{\sum_k y_{ik} \varphi_k}{\sum_k \varphi_k^2} \qquad (k = 1,2\ldots, n). \quad (4.8)$$

Using (4.8) in the left part of the eq. (4.7b), and inverting the order of the summations, we obtain n equations

$$\sum_k \varphi_k \sum_i y_{ij} y_{ik} = \varphi_j \sum_i S_i^2 \sum \varphi_k^2 \quad (4.9)$$

or

$$\sum_k R_{jk} \varphi_k = \lambda \varphi_i \quad (4.10)$$

where

$$\lambda = \frac{1}{m} \sum_i S_i^2 \sum \varphi_k^2 \quad (4.11)$$

$$R_{jk} = \frac{1}{m} \sum_i y_{ij} y_{ik}. \quad (4.12)$$

The matrix R in (4.12) is the correlation matrix

$$\|R\| = \begin{Vmatrix} R_{11} & R_{12} \ldots R_{1n} \\ R_{21} & R_{22} \ldots E_{2n} \\ R_{n1} & R_{n2} \ldots R_{nn} \end{Vmatrix}$$

The system (4.10) can be represented in the form of an eigen equation

$$(R_{11} - \lambda)\varphi_1 + R_{12}\varphi_2 + \ldots + R_{1n}\varphi_n = 0$$

$$R_{21}\varphi_n + (R_{22} - \lambda)\varphi_2 + \ldots + R_{2n}\varphi_n = 0 \quad (4.13)$$

$$R_{n1}\varphi_1 + R_{2n}\varphi_2 + \ldots + (R_{nn} - \lambda)\varphi_n = 0$$

or in the matrix form

$$(R - \lambda E)\, \varphi = 0.$$

Such a system of equations has a solution different from zero if

$$\det(R - \lambda E) = 0 \quad (4.14)$$

where λ are the eigen values, that is the roots of the algebraic equation n-eme power (4.14) (or characteristic equation). There are eigen values and n eigen vectors

$$\begin{matrix} \lambda_1 \\ \lambda_2 \\ \ldots \\ \lambda_n \end{matrix} \begin{vmatrix} \varphi_{11} \varphi_{12} \ldots \varphi_{1n} \\ \varphi_{21} \varphi_{22} \ldots \varphi_{2n} \\ \ldots\ldots\ldots\ldots \\ \varphi_{n1} \varphi_{n2} \ldots \varphi_{nn} \end{vmatrix} \quad (4.15)$$

The eigen vectors of the symmetric matrix R must be orthogonal. That is to say

$$\sum_{j=1}^{n} \varphi_{lj} \varphi_{kj} = \Delta_{lk} = \begin{cases} 0 \text{ if } l \neq k \\ 1 \text{ if } l = k \end{cases} \quad (4.16)$$

where Δ_{ik} is the Kroneker symbol (l, k = 1, 2, ..., n).

For each eigen vector we can get one complex parameter according to the formula (4.8) which becomes, after having restored the indice h

$$S_{ih} = \frac{\sum_k y_{ik}\varphi_{hk} \quad (i = 1, 2, ..., n)}{\sum_k \varphi_{hk}^2 \quad (h, k = 1, 2, ..., n)} \qquad (4.17)$$

According to the condition of orthogonality (4.16), the formula (4.17) can be written in the matrix form

$$S = y\varphi^T. \qquad (4.18)$$

Then, by finding Φ and S of eq. (4.1), we have solved the problem of the decomposition of the function $y(P, x)$ into orthogonal natural functions. According to the expression (4.18), the value of the h-complex parameter at the i-observation has the form

$$S_{ih} = \sum_{j=1}^{n} y_{ij}\varphi_{hj}. \qquad (4.19)$$

The eq. (4.19) is the result of convolution of a set of physical parameters through a complex parameter S_{ih}.

To find regularities in the variation of complex parameter S_{ih} the measurement data for each of the tested samples were split into two groups. The first included points and routes measured in macrofailure areas, the second those of the areas with no registered macrocracks.

Close interrelation between the recorded physical parameters was supposed, since all of them reflect the response of the same physical subsystem in the spatial structure of the rock. This is consistent with the high values of the correlation coefficients, *i.e.* in the range 0.6-0.98. The correlation matrices reveal invariably high correlation coefficients between acoustic parameters N and V, on the one hand, and electric $\Delta\rho$ and ΔU on other, no matter what the material.

The study of the five complex parameters S_{ih} (h = 1, 2, 3, 4, 5) computed by with account taken of concrete values of eigen vector φ_{hj}. Furthermore, our calculations showed that the bulk of information 95-98% for all analyzed cases was concentrated in the first two S_1 and second S_2, while both parameters' equations for the areas that were not brought to macrofailure differed greatly.

Table I gives the eigen vector values for the macrofailure areas in basalt block.

Coordinates of the first eigen vector, that is, of the weight function φ_1, φ_2, φ_3, φ_4, φ_5 for the parts damaged by tensile cracks are as follows: $\varphi_1 = -0.18$; $\varphi_2 = 0.23$; $\varphi_3 = -0.22$; $\varphi_4 = 0.19$; $\varphi_5 = 0.19$. For the second eigen vector, we have: $\varphi_1 = -0.25$; $\varphi_2 = -0.19$; $\varphi_3 = 0.1$; $\varphi_4 = 0.21$; $\varphi_5 = 0.22$.

The first S_1 and the second S_2 complex parameters for the points and roots measured in macrofailure areas are

$$S_1 = -0.18\,I + 0.23\,N - 0.22\,V + 0.19\,\Delta U + 0.19\,\Delta\rho$$

$$S_2 = -0.25\,I - 0.19\,N + 0.1\,V + 0.21\,\Delta U + 0.22\,\Delta\rho$$

for the basalt block and

$$S_1 = -0.10\,I + 0.23\,N - 0.15\,V + 0.24\,\Delta U + 0.23\,\Delta\rho$$

$$S_2 = -0.34\,I - 0.4\,N + 0.27\,V + 0.5\,\Delta U + 0.3\,\Delta\rho$$

for the granite block.

Table I. Eigen vectors and changes in basalt sample macrofailure areas.

Parameters	Basalt				
	1	2	3	4	5
I	– 0.18	– 0.25	– 0.35	0.12	– 0.09
N	0.23	– 0.19	0.21	0.23	– 0.07
V	– 0.22	0.1	0.08	0.32	– 0.12
ΔU	0.19	0.21	– 0.07	– 0.10	– 0.30
$\Delta\rho$	0.19	0.22	– 0.14	0.12	0.27

Despite a considerable dissimilarity in mechanical properties of granite, basalt and concrete, the complex parameters S_1 and S_2 prove morphologically identical. Typical changes in S_2 (fig. 13a,b) distinguish 3 stages of the straining of the rock. The first stage is observed at low load and is characterized by negative values of S_2 increasing to 0 (fig. 13a,b, curves 2). When the load $P \leq (0.5\text{-}0.6)P_f$ practically reversible deformation is observed. In the parts of the blocks with high strength, located far from the macrofailure zones, the quasielastic stage (*i.e.* $S_2 \leq 0$) is observed at loads up to $(0.8\text{-}0.9)P_f$. The second stage is characterized by a change in sign of S_2. It is called quasiplastic stage and corresponds to the onset of irreversible microfailures. It can be observed at loads of (0.7-0.8) P_f when S_2 reaches a maximal value and $S_1 \rightarrow 0$ (curve 2 and curve 1). In the parts of the blocks with stable deformation, the failure process does not go beyond this stage, S_{2h} (fig. 13a,b, curves 4) does not reach its maximum and S_1 (curves 3) remains negative. The third stage, called progressing macrofailure, is characterized by a sharp decrease from the maximum to negative values. The complex parameter S_1 becomes positive with accelerated increase (curves 1). For the parts of the blocks with a stable deformation, this stage is not observed.

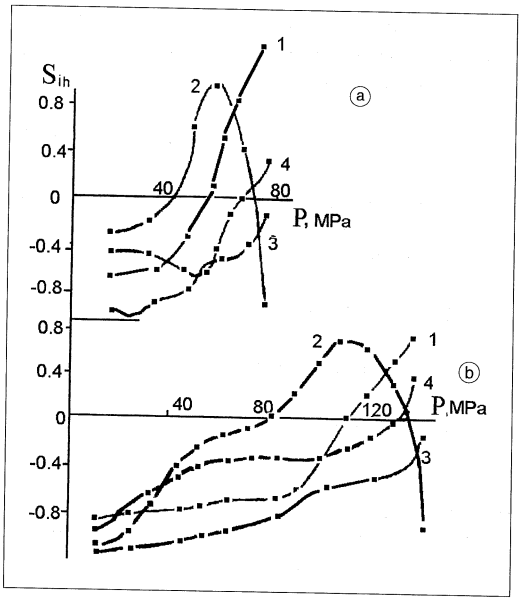

Fig. 13a,b. The variation of the complex parameters S_1 and S_2 for the basalt block (a) and granite block (b) as a function of applied stress P. 1, 2: response of the macrofailure formation zones (S_1 and S_2 respectively); 3, 4: response of for the stable deformation zones (S_1 and S_2 respectively).

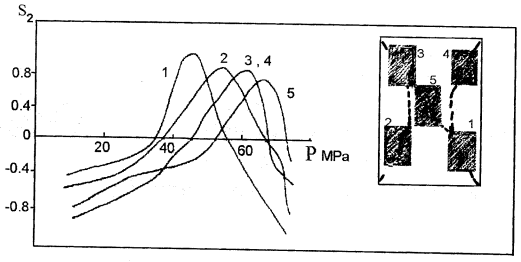

Fig. 14. Variations of the complex parameter S_2 illustrating the succession of the formation of macrofailure in the basalt block.

The increase of S_2 to a maximum, followed by a sharp decrease, combined with an increase in S_1 can be used as predictors of macrofailure in particular parts of the rock mass. The result provided in fig. 14 makes S_2 more promising in terms of prognosis.

Figure 15 shows the transition through the maximum of the complex parameter S_2 in five zones of the basalt block in which cracks appeared. The displacement of the point of maximum S_2 from 1 to 5 reflects the evolution of the failure process. Curves 3 and 4 are clearly identical because the cracking occurred almost at the same time in these 2 zones. Figure 16a shows S_2 for the third loading cycle of the large concrete block, suggesting that the central element (4), that is, the barrier between the concentrators, was not yet damaged because the curve (4) corresponding to this domain had not yet reached a maximum. The macrorupture in this zone took place during the fourth cycle of loading when the elements 5, 6 and 4 located between the elements 4, 3, progressively failed (fig.16b). Thus the rupture migrated from the vicinity of the concentrators towards the center of the barrier.

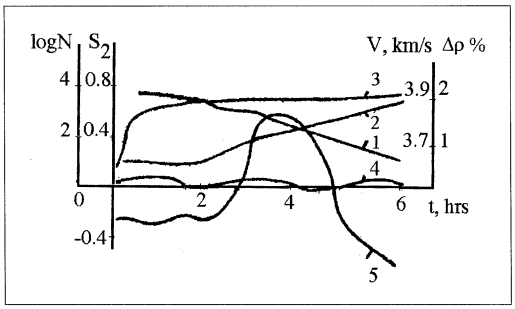

Fig. 15. Comparison of different physical precursors during the basalt experiment. 1 = longitudinal elastic wave velocity; 2 = local longitudinal deformation; 3 = acoustic emission intensity; 4 = relative variation of electrical resistivity; 5 = complex parameter S_2 behaviour prior to macrofailure in basalt block.

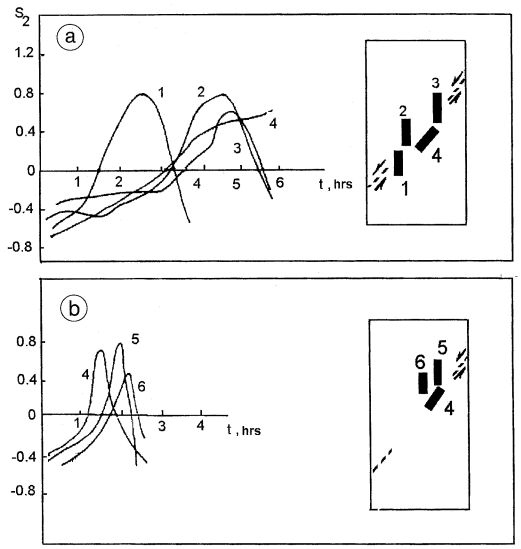

Fig. 16a,b. Variations of the complex parameter S_2 illustrating the succession of the formation of macrofailure in the concrete pattern during its third cycle (a) and its fourth load cycle (b).

In practice, it is interesting to try to decrease the number of physical parameters used to calculate S_1 and using various combinations of 4, 3 and 2 physical recorded parameters, S_2 and S_1 were calculated. When only 2 physical parameters are used, the prediction power of S_2 practically disappears. Prediction of the approaching macrofailure is then possible only through S_1. The informativity of S_2 and S_1 is always sufficient to detect all three stages using four or three acoustic and electric parameters. This property makes it possible to automatically control the state of the block and predict catastrophic phenomena in different parts of it. This should also give us some insight into the problem of optimization of the number of recorded geophysical parameters in order to forecast earthquakes.

5. Conclusions

The results of our observations on large rock blocks, enable us to assert that forecasts of macrofailure in real time can be made. The number of various precursors increases as the time of failure approaches, thus enhancing the reliability of forecasting the time and location of a macrorupture. The important thing to emphasise is that the well-known phenomenon of a distribution of precursors is an inevitable consequence of the development of localized deformation itself, not merely a consequence of inhomogeneous structure of the medium. The anomalies' physical parameters, located in space and time, were caused by coalescing ruptures and the formation of failure fractal structure. These anomalies have certain characteristics in common, such as passage through an extremum or increased prefailure dispersion. In certain zones, velocity and resistivity anisotropies were found to develop with time. An anomalous change in time-space of these physical parameters reflects various deformation stages and formation of hierarchic structures. That shows the perspectives of the use of this approach for the further development of studies on seismic prediction.

The complex statistical parameter S_{ih} effectively summarizes information on a series of physical (mechanical and electrical) failure precursors of a strained rock. S_{ih} has a wide range of variation, depending on the stress and strain state of the rock. It can therefore be used for the diagnosis of near failure state of the block and prediction of its failure. Change in S_2 indicates

that the rock stress-strain states could be divided into three stages: quasielastic; quasiplastic; and finally the progressing macrofailure stage. The complex parameter S_1 is used to confirm the transition to the progressing failure stage. The transition of S_2 over the maximum and the rapid increase in S_1 are effective as predictors of approaching brittle macrofailure. On the whole, the stated examples of parameter processing demonstrate that the analysis of a set of physical fields makes the job of precursor identification much more unambiguous and practically dependable. Hopefully, similar ways of processing, backed by multidimensional mathematical analysis will prove as promising for field observation data meant for earthquake prediction.

If the models described above have some similarity with the real situation in the Earth, for example, in the areas of seismic gaps, these results then strengthen the physical basis of earthquake and rockburst prediction.

REFERENCES

BADDARI, K. and A.D. FROLOV (1995): Modeling of mechanics and precursors of superficial earthquakes of seismoactive region, Moscow, *Izv. Vouz. Gueologuia i Razvedka*, **1**, 102-108.

BADDARI, K. and A.D. FROLOV (1997): Modelisation de la structure fractale d'un milieu géophysique, *C. R. Acad. Sci., Paris*, **325**, 925-930.

BADDARI, K., G.A. SOBOLEV and A.D. FROLOV (1988): Complex precursors in large rock blocks failure, *DAN SSSR*, **299** (5), 1087-1091.

FROLOV, A.D. (1986): Rock is a complex macrosystem, *Vsesoyouzn. Conf. Systemy Podkhod ve Gueologui*, abstract, Ch. 1, Moscow.

HOROWITZ, F. and A. RUINA (1989): Slip patterns in spatially homogenous fault model, *J. Geophys. Res.*, **94**, 10279-10298.

LEI, X., O. NISHIZAWA, K. KUSUNOSE and T. SATOH (1992): Fractal stucture of the hypocenter distribution and focal mechanism solutions of acoustic emission in two granites of different grain sizes, *J. Phys. Earth*, **40**, 617-634.

LOCKNER, D.A., and J.D. BYERLEE (1991): Precursory AE patterns leading to rock fracture, in *Proceedings 5th Conference Acoustic Emission/Microseismic Activity in Geological Structure and Material*, Pennsylvania State University, 1-14.

LOCKNER, D.A, J.D. BYERLEE, V.S. KUKSENKO, A. PONOMAREV and A. SIDORIN (1991). Quasistatic fault growth and shear fracture energy in granite, *Nature*, **350** (6313), 39-42.

MEREDITH, P.G., G. MAIN and C. JONS (1990); Temporal variations in *m*-valus of rock failure and mechanic properties of the rock, *J. Seismol. Res.*, **13**, 291-297.

NIKITIN, A.A. (1993); Statistical processing of geophysical data, in *Advanced Geophysics, Russian Experience*, Moscow, Electromagnetic Research Center, pp. 115.

OHNAKA, M. and Y. KUNWAHARA (1990); Characteristic features of local brekdown near a crack-tip during stick-slip near failure, *Tectonophysics*, **175**, 197-220.

RICE, J. (1983); Constitutive relations for fault slip and earthquake instabilities, *Pure Appl. Geophys.*, **121**, 187-219.

SAVICH, A.I. (1983-1984); A study of physical and mechanical properties of rocks at different scale levels, *Prognoz zemletryasenii*, **4**, 273-288.

SOBOLEV, G.A. (1993); *Fundamental of Earthquake Prediction* (Moscow, Nauka), pp. 313.

SOBOLEV, G.A. and K.O. ASATRIAN (1990); Hierarchical evolution of fracturation during the deformation of very plastical materials, *Dokl. Akad. Nauk USSR*, **315** (2), 345-348.

SHOLZ, C., P. MOLNAR and T. JOHNSTON (1972): Detailed studies of frictional sliding of granite and implications for earthquake mechanisms, *J. Geophys. Res.*, **77**, 6392-6406.

ZHAOYONG, X., G. NAIGUANG and M. SHIRONG (1990): Acoustic emission *m*-valus of rock failure and mechanic properties of the rock, *J. Seismol. Res.*, **13**, 291-297.